

A Comprehensive Catalog of Emission-line Nebulae, Star Clusters, and Supergiants in M31 from the LAMOST Spectroscopic Survey

PINJIAN CHEN ^{1,2,3} BINGQIU CHEN ⁴ XUAN FANG ^{3,2,5,6} HAIBO YUAN ^{7,8} BAISONG ZHANG ⁴
XIANGWEI ZHANG ^{3,2} JIARUI SUN ⁹ AND XIAOWEI LIU ⁴

¹Department of Astronomy, Yunnan University, Kunming 650500, Yunnan, P. R. China

²School of Astronomy and Space Science, University of Chinese Academy of Sciences, Beijing 100049, P. R. China

³CAS Key Laboratory of Optical Astronomy, National Astronomical Observatories, Chinese Academy of Sciences, 20A Datun Road, Beijing 100101, P. R. China

⁴South-Western Institute for Astronomy Research, Yunnan University, Kunming 650500, Yunnan, P. R. China

⁵Xinjiang Astronomical Observatory, Chinese Academy of Sciences, 150 Science 1-Street, Urumqi, Xinjiang 830011, P. R. China

⁶Laboratory for Space Research, Faculty of Science, The University of Hong Kong, Pokfulam Road, Hong Kong, P. R. China

⁷School of Physics and Astronomy, Beijing Normal University, Beijing 100875, P. R. China

⁸Institute for Frontiers in Astronomy and Astrophysics, Beijing Normal University, Beijing 102206, P. R. China

⁹Department of Astronomy, School of Physics and Astronomy, Shanghai Jiao Tong University, Shanghai 200240, P. R. China

ABSTRACT

Spectroscopic observations of various tracers in nearby galaxies, such as Andromeda (M31), play a crucial role in identifying and classifying individual stellar populations and nebular objects, thereby enhancing our understanding of galactic composition, environment, and dynamics as well as stellar evolution. While the LAMOST (Large Sky Area Multi-Object Fibre Spectroscopic Telescope) survey of M31 has produced extensive datasets, a comprehensive catalog of emission-line nebulae, star clusters, and supergiants is yet to be completed. In this paper, we present a final catalog of 384 emission-line nebulae, 380 star clusters, and 375 supergiants and candidates in M31, as carefully selected and identified from the LAMOST spectroscopic database. These objects were classified using a random forest algorithm, followed by thorough visual examinations of their spectral characteristics as well as morphologies revealed by archive images. For emission-line nebulae, we measured radial velocities and relative fluxes of emission lines, enabling further classification of planetary nebulae and H II regions. Additionally, we identified 245 emission-line nebulae in M33. This work lays the data foundation for the study of M31, and offers valuable tracers to investigate M31's structure and evolution.

Keywords: Galaxies: individual (M31, M33) — planetary nebulae: general — H II regions — star clusters — supergiants — catalogs

1. INTRODUCTION

The Andromeda Galaxy (M31), our closest large disk neighbor, is located approximately 780 kpc away (Holmberg 1998) and is the brightest and likely the most massive member of the Local Group. At a slightly greater distance of 809 kpc (McConnachie et al. 2005), the Triangulum Galaxy (M33) ranks as the third-largest member of the Local Group, after M31 and the Milky Way (MW). Their proximity and brightness make M31

and M33 ideal environments for studying astrophysical processes, including stellar evolution, the interstellar medium, and the formation and evolution of galaxies. Individual objects in these galaxies can be detected and studied with high precision, providing valuable insights into these processes.

Identifying and classifying the various components of large spiral galaxies like M31 and M33 is essential for understanding galaxies similar to our own. While progress has been made over many decades, it remains a foundational challenge. Star clusters, for instance, have long been used as tracers of the global properties and formation history of M31. Edwin Hubble first identified 140 globular clusters (GCs) likely associated with M31

(Hubble 1932). Later, Galleti et al. (2004) updated the Bologna catalog (Battistini et al. 1987), expanding it to include 693 known and candidate GCs, using data from the Two Micron All Sky Survey (2MASS; Cutri et al. 2003), leading to the Revised Bologna Catalog (RBC). More recently, high-resolution images from the Pan-Andromeda Archaeological Survey (PANdAS; McConnachie et al. 2009) have further advanced the discovery of GCs and their candidates in M31 (Huxor et al. 2014; Veljanoski et al. 2014), with machine learning techniques offering even greater precision (Wang et al. 2022, Wang et al. 2023, Zhang in preparation).

Similarly, emission-line objects in M31 have been extensively cataloged. Merrett et al. (2006, hereafter M06) compiled a comprehensive catalog of 3,300 emission-line objects in M31, of which 2,615 are likely planetary nebulae (PNe). A more recent imaging survey of a 54-square-degree area centered on M31 increased the total number of PNe and candidates to 5,625 (Bhattacharya et al. 2019, 2021), although only a fraction of these have been confirmed through spectroscopy (Bhattacharya et al. 2022).

In addition, large photometric surveys, such as the Local Group Galaxies Survey (LGGS; Massey et al. 2006), have provided opportunities to search for massive stars. Using radial velocity data, Massey et al. (2009) and Drout et al. (2009, 2012) successfully distinguished red and yellow supergiants in M31 and M33 from foreground MW stars. More recently, Ren et al. (2021, hereafter R21) identified a significant sample of red supergiants in M31 and M33 using near-infrared color diagrams.

The development of wide-field, large-scale spectroscopic surveys has greatly expanded our ability to study extragalactic systems. The Large Sky Area Multi-Object Fiber Spectroscopic Telescope (LAMOST; Cui et al. 2012), with its 4000 robotic fibers and 20 deg² field of view, is particularly well-suited for spectroscopic surveys of individual objects in M31. Several pioneering studies have used LAMOST data to study emission-line nebulae (e.g., PNe and H II regions, Yuan et al. 2010; Xiang et al. 2017; Zhang et al. 2020), GCs (Chen et al. 2015, 2016; Wang et al. 2021), and massive stars (Huang et al. 2019; Liu et al. 2022; Wu et al. 2024) in M31. However, although LAMOST has completed its first- and second-phase surveys, and M31 is not included in future observation plans, a comprehensive catalog of M31 objects from LAMOST data remains unpublished. This paper aims to address this gap.

Due to LAMOST’s limiting magnitude, only the brightest objects in M31 can be observed spectroscopically within a reasonable time frame. Consequently, our study focuses on three types of objects: emission-

line nebulae, star clusters, and supergiants. These objects are excellent tracers for studying the chemical composition, kinematics, and stellar populations of their host galaxies. We applied a Random Forest classifier for an initial categorization of these objects. For those that could not be definitively classified based on spectra alone, we conducted a kinematic analysis. During this process, we also identified several emission-line nebulae in M33 as part of the byproduct of this work.

2. LAMOST SPECTROSCOPIC SURVEY DATA

The LAMOST pilot survey was completed in June 2012, followed by a five-year first-phase survey and a subsequent five-year second-phase survey. In the first phase, only low-resolution ($R \sim 1800$) spectroscopy was carried out, whereas in the second phase both low-resolution and medium-resolution ($R \sim 7500$) observations were made. Our study is based on the LAMOST DR9 v1.0 data release¹, publicly available in 2022 April. This data release includes both low- and medium-resolution spectra observed between 2011 October and 2021 June.

For this work, we focus on the low-resolution spectroscopic catalog, selecting the sky region within 15 degrees centred on M31. This selection provided us with 648,485 spectra corresponding to 466,680 unique sources. We also incorporated spectra from earlier LAMOST low-resolution catalogs. These include low signal-to-noise (S/N) spectra that the LAMOST 1D pipeline could not classify (Luo et al. 2015), leading them to be labeled as “Unknown”. In some cases, nebular spectra with minimal continuum may have been misclassified by the pipeline, prompting us to search for potential emission-line nebulae within this subset. This additional step contributed 2,950 spectra from 2,721 unique objects in the vicinity of M31 and M33.

In total, our initial sample consisted of 651,435 spectra from 469,401 distinct objects. These spectra cover a wavelength range of $\sim 3700\text{--}9100 \text{ \AA}$, with a resolution of $R \sim 1800$ at 5500 \AA .

3. INITIAL SEARCH FOR M31 OBJECTS USING RANDOM FOREST CLASSIFIERS

The Random Forest (RF) algorithm is a robust supervised machine learning technique commonly used for both classification and regression tasks (Breiman 2001). To identify potential candidates of M31 objects, we employed RF as the first step of our method, specifically utilizing the Random Forest Classifier (RFC). RF enhances predictive accuracy by utilizing a large ensemble

¹ <http://www.lamost.org/dr9/v1.0/>

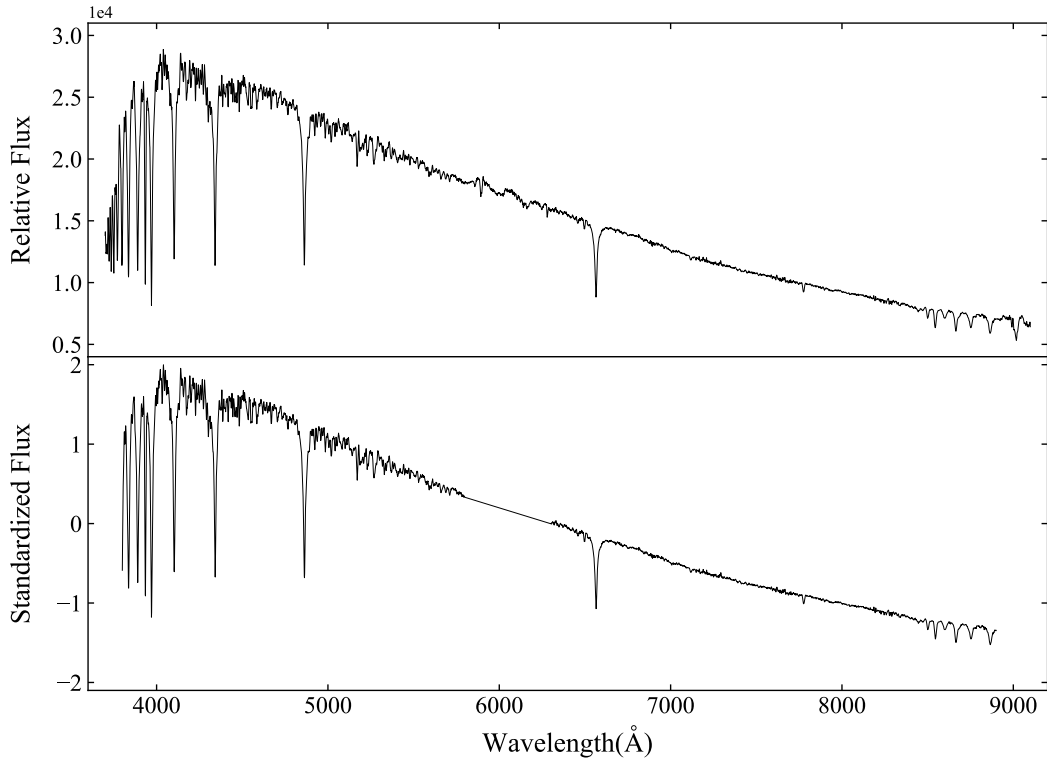


Figure 1. Top panel: the original LAMOST spectrum of an A-type star. Bottom panel: the same spectrum after preprocessing. The spectrum in the wavelength region 5800–6300 Å, where the LAMOST blue and red arms are connected, is masked using a straight line.

of decision trees. Each tree is constructed using a randomly selected subset of the training data, generated through bootstrapping, and a randomly chosen subset of features. The model’s performance is optimized by minimizing the error function (in this case, the Gini index), and the final prediction is made by averaging the results from all trees in the ensemble.

3.1. The Training Sample

The effectiveness of RFC depends on the quality of the training sample. To build a comprehensive and reliable dataset, we collected sources from several catalogs, ensuring both high completeness and minimal contamination. Our search extended beyond the SIMBAD database to include emission-line objects from M06, star clusters and candidates from the Revised Bologna Catalogue version 5 (RBC V5)² and Chen et al. (2015, hereafter C15), as well as red supergiants from R21. We also incorporated online resources such as “PNe in M31”, “HII regions in M31”, “Just star clusters in M31”, and

“Stars in the M31 catalog”, all contributed by Nelson Caldwell³.

We cross-matched these catalogs with our selected LAMOST catalog within a 3'' radius and visually inspected each spectrum. Based on spectral features, we classified the objects into three categories: stars without emission lines (class 0), emission-line objects (class 1), and star clusters (class 2). Class 0 included both foreground Galactic stars and supergiants without emission lines from M31 and M33, while class 1 comprised emission-line nebulae and emission-line supergiants within these galaxies. Class 2 consisted of both young and old star clusters in M31 and M33. For candidate objects from the literature, we applied the same classification criteria as those used for confirmed objects.

We excluded from the training sample the LAMOST spectra with low S/N, missing data, or any contaminations. Additionally, objects labeled as “Unknown” were discarded at this stage due to the absence of radial velocity information. After this filtering process, our initial

³ <https://web.cfa.harvard.edu/oir/eg/m31clusters/M31-Hectospec.html>, accessed on 4th September 2022.

² <http://www.bo.astro.it/M31/>

Table 1. Precision, Recall, and F1 Scores of Our Trained RFC for All Classes

Class	Precision	Recall	F1 score
Class 0	0.94	0.94	0.94
Class 1	0.91	0.93	0.92
Class 2	0.91	0.89	0.90

training sample comprised 38,522 spectra for class 0, 370 spectra for class 1, and 604 spectra for class 2.

3.2. Data Preprocessing and Model Training

To input data into the RFC, the data must be numerical. In the current work, we used the fluxes at individual wavelengths as input features. First, we applied linear interpolation to the redshift-corrected LAMOST spectra, limiting the rest-frame wavelength range to 3800 Å to 8900 Å. To avoid potential misalignments, we excluded the wavelength region between 5800 Å and 6300 Å, where the blue and red arms of the spectrum connect. Subsequently, we performed standard z-score normalization, defined as:

$$Z = \frac{F - \mu}{\sigma}, \quad (1)$$

where F represents the flux, μ is the mean flux of the spectrum, and σ is the standard deviation. This process transformed the original spectra into a 4100×1 array. Fig. 1 shows an example of both the original and pre-processed spectra.

RF performs optimally when trained on balanced datasets (Breiman 2001). To achieve this, we randomly split the dataset into two parts: 80% for training and 20% for testing. To enhance the training set, we applied noise augmentation by adding Gaussian noise to the flux values based on the “IVAR” (inverse variance) values provided by LAMOST. For data points without inverse variance information, we used the mean value of the entire spectrum. The final balanced training set contained 30,820 spectra for class 0, 31,096 spectra for class 1, and 30,528 spectra for class 2.

We employ the SCIKIT-LEARN package for PYTHON (Pedregosa et al. 2011) to train the RFC models. The GridSearchCV function is first adopted to optimize the most relevant hyperparameters for the Random Forest model. The final configuration included $n_estimators = 500$, $max_depth = 30$, and $max_features = 500$. All other hyperparameters were left at their default values. To assess the model’s performance, we used the F1 score and a confusion matrix. The F1 score is the harmonic mean

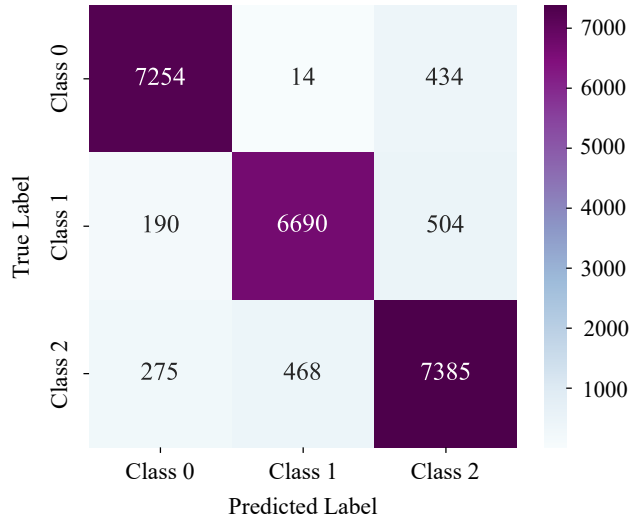


Figure 2. Confusion matrix showing the predicted and true classifications from the trained RFC.

of precision and recall, ranging from 0 to 1. For multi-class classification, the F1 score for each class is defined as:

$$F1_i \text{ score} = 2 \cdot \frac{P_i \cdot R_i}{P_i + R_i}, \quad (2)$$

where P_i is the precision and R_i is the recall for class i . Precision and recall are given by:

$$P_i = \frac{TP_i}{TP_i + FP_i}, \quad R_i = \frac{TP_i}{TP_i + FN_i}, \quad (3)$$

where TP_i is the number of true positives for class i , FP_i is the number of false positives, and FN_i is the number of false negatives. The resulted precision, recall, and F1 scores of our trained RDC model for the individual classes are shown in Table 1, and the confusion matrix is displayed in Fig. 2. Our model achieved an overall accuracy of 92%.

4. FURTHER CLASSIFICATION OF CANDIDATES

To minimize contamination from background galaxies and quasars, we excluded LAMOST spectra with radial velocities exceeding 2,000 km s⁻¹. We also removed spectra labeled as “Unknown” and those with erroneous redshift values (e.g., -9,999). These targets will be discussed in detail later (see Sect. 4.2). The remaining spectra, which were not part of the training sample, were classified using our trained RFC model. This procedure resulted in the classification of 418,850 spectra as class 0, 9,284 as class 1, and 183,623 as class 2. Example spectra for each of these object types are shown in Fig. 3.

We performed a preliminary review of the spectra classified as class 1. The majority of these spectra displayed prominent H α emission lines, though some were affected

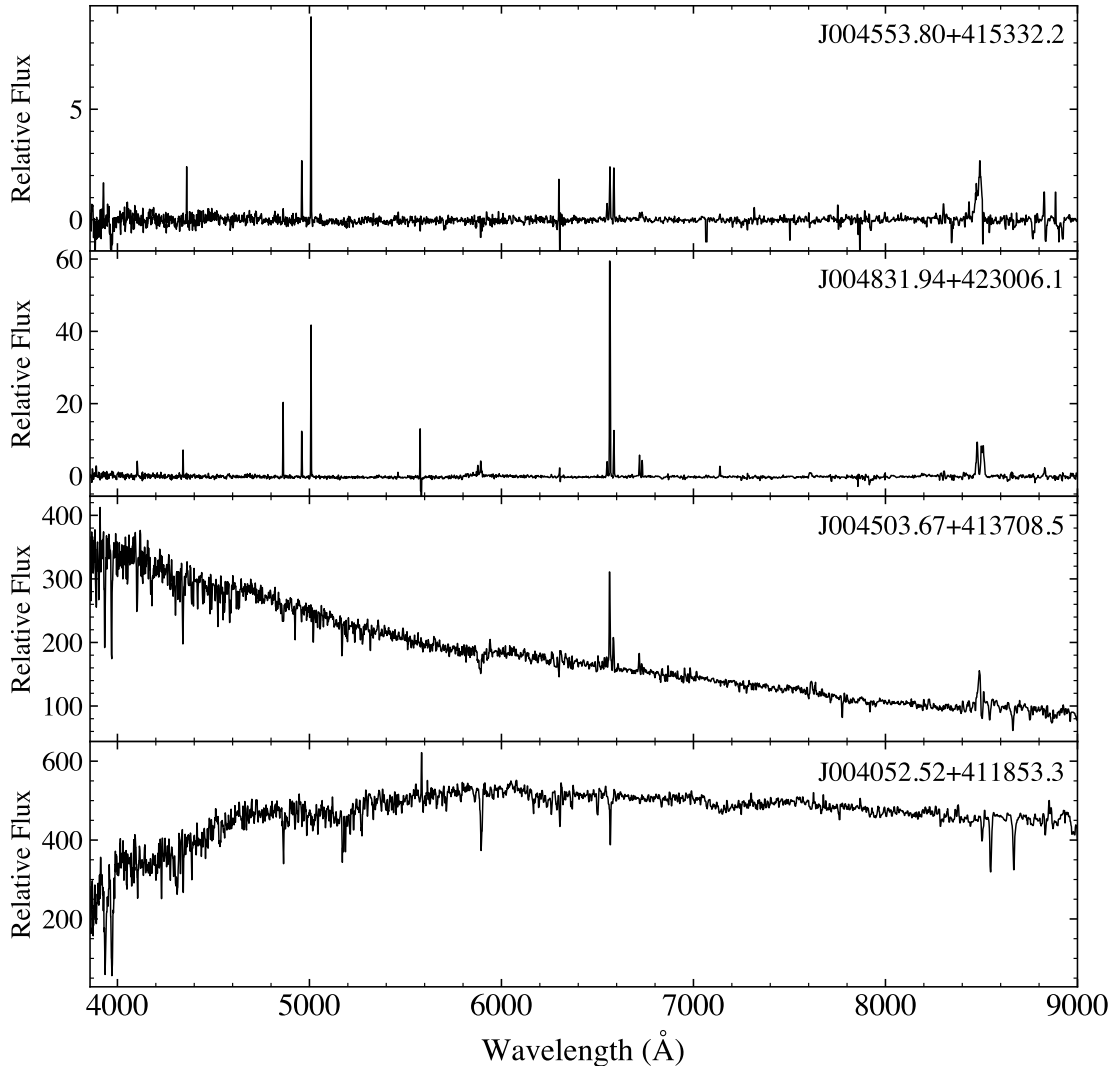


Figure 3. Examples of LAMOST spectra of the targets cataloged in this work, smoothed by 3 pixels. From top to bottom: a PN candidate from M06, a newly discovered H II region candidate, a newly discovered yellow supergiant candidate, and a known globular cluster from RBCV5.

by low S/N or cosmic rays. We first removed the low-quality spectra from further analysis. Additionally, we noted that a significant portion of the class 1 candidates were M-type dwarfs, characterized by strong TiO and VO molecular bands. These objects were identified as foreground stars, as their intrinsic faintness makes them too dim to be detected by LAMOST at the distance of M31. Consequently, we excluded these spectra from further consideration.

Moreover, we identified a clustering of objects in the northern sky region of our sample. Upon reviewing available H α images from the Virginia Tech Spectral Line Survey (VTTS; Dennison et al. 1998), we concluded that the nebular lines in these spectra originated from the ionized interstellar medium (ISM) of the Galactic

foreground. As a result, we discarded these targets with $\delta > 45^\circ$.

The remaining spectra were carefully inspected. In most cases, those exhibiting strong absorption lines were classified as emission-line stars, while spectra with minimal continuum were identified as emission-line nebulae. However, the relatively large fiber diameter of LAMOST introduces the possibility of contamination from the bright continuum background of M31, especially near the spiral arms and central bulge. Therefore, we allowed more leniency for objects with strong emission lines in these regions. Determining membership for emission-line stars based solely on spectra with relatively low S/N remains difficult, and further classification is postponed. This will be addressed alongside radial velocity

data in Section 4.1. Ultimately, our analysis identified 128 unique objects as emission-line nebulae.

Unexpectedly, the RFC model classified a large number of objects as class 2, suggesting they may be star clusters. By applying a probability threshold of 0.95, we obtained a sample of 2,482 unique objects. For these candidates, we examined their morphologies using high-resolution g - and i -band images from the PAndAS archive. However, none of the sources exhibited obvious extended structures. Thus, the class 2 candidates are predominantly stars, particularly those without emission lines.

4.1. Kinematic Selection of Supergiants in M31

M31 provides an excellent environment for studying supergiant populations and testing massive star evolutionary models. The main challenge in identifying supergiants within M31 is distinguishing them from foreground MW stars. For red supergiants, the two-color method (e.g., Ren et al. 2021; Massey et al. 2021) is effective in removing foreground stars. However, this approach is less effective for blue and yellow supergiants. For these objects, a common strategy is to first select candidates based on color-magnitude diagrams and then compare their radial velocities with expected values (e.g., Massey et al. 2009; Drout et al. 2009; Massey & Evans 2016). In this study, we adopted this latter method to identify M31 supergiants.

The radial velocity of an object in the disk plane of a spiral galaxy can be estimated using the relation $V_r = V_{\text{sys}} + V(R_{\text{gal}}) \sin \xi \cos \theta$ (Rubin & Ford 1970), where V_{sys} is the systemic radial velocity, $V(R_{\text{gal}})$ is the circular velocity at a deprojected galactocentric distance R_{gal} , ξ is the angle between the line of sight and the normal direction of the galactic disk plane, and θ is the azimuthal angle in the disk plane. With $\cos \theta = X/R_{\text{gal}}$, where X represents the position along the major axis, a flat rotation curve ($V(R_{\text{gal}}) = \text{const}$) results in a linear relationship between V_r and X/R_{gal} . To compute the expected radial velocity V_{exp} , we used the relation from Massey & Evans (2016):

$$V_{\text{exp}} = -311.8 + 242.0(X/R_{\text{gal}}), \quad (4)$$

which was derived from fitting the radial velocities of a large sample of red supergiants in M31. This relation differs by roughly 17 km s^{-1} from the result obtained by Drout et al. (2009).

To assess the likelihood of an object belonging to M31 or the MW, we first compiled samples of both types from the LAMOST data. Known M31 objects were drawn from our catalogs of emission-line nebulae, star clusters, and stars, including supergiants and candidates

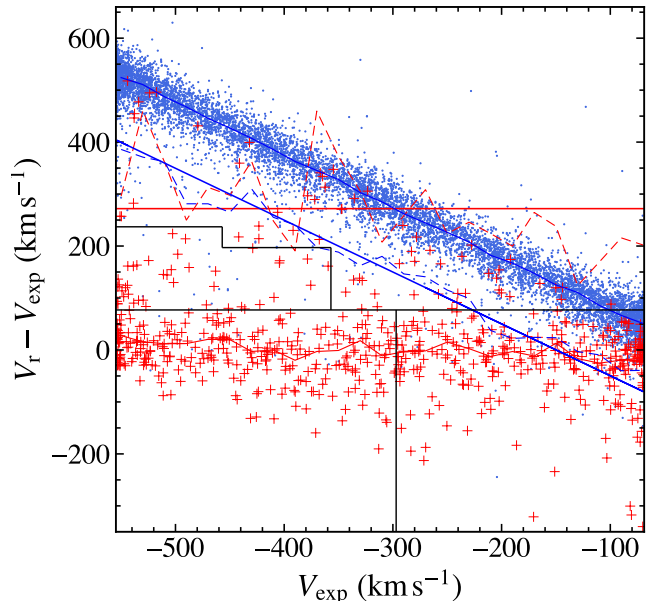


Figure 4. Comparison of the radial velocities, observed (V_r) and expected (V_{exp}), for M31 and MW objects, represented by red crosses and blue dots, respectively. The velocity difference ($V_r - V_{\text{exp}}$) is plotted against V_{exp} . The median values of velocity difference for M31 and MW objects are shown by the red and blue solid curves, respectively, with the red- and blue-dashed curves representing the 3σ scattering of data points. The red-solid straight line indicates a constant $V_r - V_{\text{exp}} = 271.9 \text{ km s}^{-1}$ for M31 objects, and the blue-solid straight line shows $V_r = -149.5 \text{ km s}^{-1}$ for the MW objects. The black lines indicate the criteria (after correction) given by Drout et al. (2009).

identified in previous studies. These objects were required to have a galactocentric distance between 1 and 25 kpc to ensure sufficient rotational support. We excluded “high-velocity” tracers according to the criteria from Kafle et al. (2018). For emission-line nebulae, we used the radial velocities measured in our analysis, while “Unknown” nebulae were excluded due to their ambiguous nature. We visually inspected the radial velocities of all objects and removed any with poor-quality data. For objects with multiple observations, we selected the velocity measurement from the spectrum with the highest S/N. MW objects were selected from the SIMBAD database and classified as “Star” with $R_{\text{gal}} < 200 \text{ kpc}$. This yielded 661 M31 objects and 9,651 MW objects.

We calculated the expected radial velocities for all objects using Equation 4, and the parameters of M31 used in this calculation are listed in Table 2. Fig. 4 shows the kinematic distribution of these objects, along with the criteria from Drout et al. (2009), adjusted by 17 km s^{-1} for V_{exp} . M31 objects, which are expected to exhibit significant disk rotation, should be located near

Table 2. Parameters of M31 Adopted in This Work

Parameter	Value	Ref.
R.A. (J2000)	00 ^h 42 ^m 44.33 ^s	[1]
Decl. (J2000)	+41°16′07.5″	[1]
Position Angle	38°	[2]
Inclination Angle	77°	[3]
Distance	780 kpc	[4]
Heliocentric Radial Velocity	−300 km s ^{−1}	[5]

References: [1] de Vaucouleurs (1959); [2] Kent (1989); [3] Walterbos & Kennicutt (1987); [4] Holland (1998); [5] de Vaucouleurs et al. (1991)

the $y = 0$ position, while foreground MW sources should align along the line representing $V_r = 0$.

We divided the V_{exp} range from -560 to -60 km s^{−1} into 25 bins and calculated the median and standard deviation for both M31 and MW objects in each bin. These values were then used to define two Gaussian probability functions. The first Gaussian, $\mathcal{N}_{\text{M31}}(\mu_1, \sigma_1^2)$, represents M31 objects with a mean $\mu_1 = 0.4$ km s^{−1} and a standard deviation $\sigma_1 = 90.5$ km s^{−1}. The second Gaussian, $\mathcal{N}_{\text{MW}}(\mu_2, \sigma_2^2)$, describes MW objects with a mean $\mu_2 = -V_{\text{exp}} - 23.2$ km s^{−1} and a standard deviation $\sigma_2 = 42.1$ km s^{−1}.

Despite restricting our M31 sample to objects in the disk, some halo objects such as GCs and PNe located in the halo but projected onto the disk are inevitably included. These objects tend to exhibit a kinematic distribution characterized by a straight line, $V_r - V_{\text{exp}} = -V_{\text{exp}} - 300$ km s^{−1}, with large dispersion. This is evident in Fig. 4, where red pluses appear in the upper-left and lower-right quadrants. A few M31 stars are also found in the upper-left region, likely belonging to the MW based on their kinematics (see Sect. 5.3). Similarly, some MW objects may be misclassified as M31 stars in the SIMBAD database, but the uncertainty introduced by such misclassifications is expected to be less than 10 km s^{−1} and is considered negligible.

Supergiants in M31, located near the top of the Hertzsprung-Russell (HR) diagram, are among the few bright stars detectable by LAMOST due to its magnitude limit ($r \sim 19$ mag). To identify supergiant candidates, we selected objects classified as class 1 and class 2 by the RFC model, along with those identified as emission-line stars. We also included objects classified as “Star” in the SIMBAD database due to their ambiguous membership. However, we excluded 14 objects previously identified as foreground dwarfs or subgiants by Gordon et al. (2016). All objects were required to

have a galactocentric distance within 25 kpc to the center of M31. The probabilities of each object belonging to M31 or the MW were estimated using the Gaussian probability density functions and scaled to a range of 0 to 1. Supergiant candidates were selected based on the following criteria:

1. P_{M31} falls within the 3σ range of $\mathcal{N}_{\text{M31}}(\mu_1, \sigma_1^2)$,
2. P_{MW} lies outside the 3σ range of $\mathcal{N}_{\text{MW}}(\mu_2, \sigma_2^2)$.

Using these criteria, we identified 248 unique supergiant candidates.

Though LAMOST also covers M33, the smaller systemic velocity of M33 (~ -179 km s^{−1}; de Vaucouleurs et al. 1991) reduces the “blank” region between the red and blue curves in Fig. 4, which we use to distinguish between M31 objects and MW stars. As a result, this method would likely suffer from significant foreground contamination, so we do not extend our supergiant selection to M33 in this work.

Furthermore, we note that the kinematic method used to select supergiant candidates is ineffective in a small region of M31’s northeastern disc. In this area, the expected radial velocities overlap with the velocities of foreground disk stars (see Fig. 4). To address this, we visually examined the LAMOST spectra in this region. Fortunately, we identified a yellow supergiant candidate, LAMOST J004503.67+413708.5, based on its spectral features. The spectrum has sufficient S/N to clearly reveal luminosity-sensitive lines, including the Ti II and Fe II blends, as well as the O I $\lambda 7774$ triplet (see Fig. 3).

4.2. Further Visual Examination of the “Unknown” Spectra Classified by LAMOST

The primary objective of this step is to identify the emission-line nebulae with their spectra classified as “Unknown” by the LAMOST pipeline. These spectra could not be categorized by the RFC model, as the absence of reliable redshift information prevents us from shifting them to the specific rest-frame wavelength range required for our analysis. Most of these spectra exhibit very low S/N and could not be successfully cross-matched with LAMOST spectral templates. Therefore, we focused only on spectra with strong emission lines.

Following a thorough visual inspection, we unexpectedly identified 309 emission-line nebulae in the vicinity of M31 and M33. This number closely matches the total number of the nebulae identified in the DR9 sample. Moreover, we discovered seven objects projected onto the disc of M31 that exhibit H α emission lines with broad wings in their spectra. This feature in line profile is commonly observed in massive supergiants and is attributed to Thomson scattering and other related mech-

anisms (Bernat & Lambert 1978; Hillier 1991). Based on these characteristics, we propose these seven objects as supergiant candidates.

To distinguish between previously known and newly identified objects, all candidates selected from the LAMOST “Unknown” spectra were cross-matched with the catalogs described in Section 3.1, following the same procedure.

5. RESULTS AND DISCUSSION

5.1. Emission-Line Nebulae

We compiled a comprehensive catalog of emission-line nebulae from LAMOST data, encompassing 629 unique objects. In M31, the sample includes 102 known planetary nebulae (PNe), 122 PN candidates, 62 previously identified H II regions, 76 candidates, and 22 unclassified nebulae. In M33, the catalog includes 30 known PNe, 15 candidates, 95 known H II regions, 88 candidates, and 17 unclassified emission-line nebulae. Table 3 lists each object’s ID, position, radial velocity, emission-line ratio, and final classification.

Given the relatively low S/N of many LAMOST spectra, we conservatively labeled new discoveries as candidates, though some classifications are highly plausible. After cross-referencing with the SIMBAD database and relevant literature, we identified 32 PN candidates and 70 candidate H II regions near M31 as new discoveries. In M33, we found 6 PN candidates and 84 H II region candidates. The term “new” refers to objects that, to the best of our knowledge, have no prior identification within a $3''$ radius. For some ambiguous objects from the literature, we updated their classifications based on LAMOST spectra. For instance, several PN candidates from M06 were reclassified as more likely being H II regions. Recently, Alexeeva & Zhao (2022) presented a catalog of 95 H II regions and 15 PNe in M33 using LAMOST DR7 data. While our catalog further expands the number of emission-line nebulae in M33, it includes the majority of objects in their work, with only a few excluded due to broad emission lines, suggesting they may be massive supergiants.

Another more recent catalog was reported by Bosomworth et al. (2024), who spectroscopically identified 294 H II regions in M31 using the Hectospec spectrograph on the 6.5-m Multi-Mirror Telescope (MMT). We cross-matched our catalog with that of Bosomworth et al. (2024) and found 26 objects in common, of which 24 have consistent classifications. Of the remaining two objects, one was classified as an “Unknown” emission-line nebula due to low S/Ns of its LAMOST spectrum, and the other one has been classified as a PN candidate

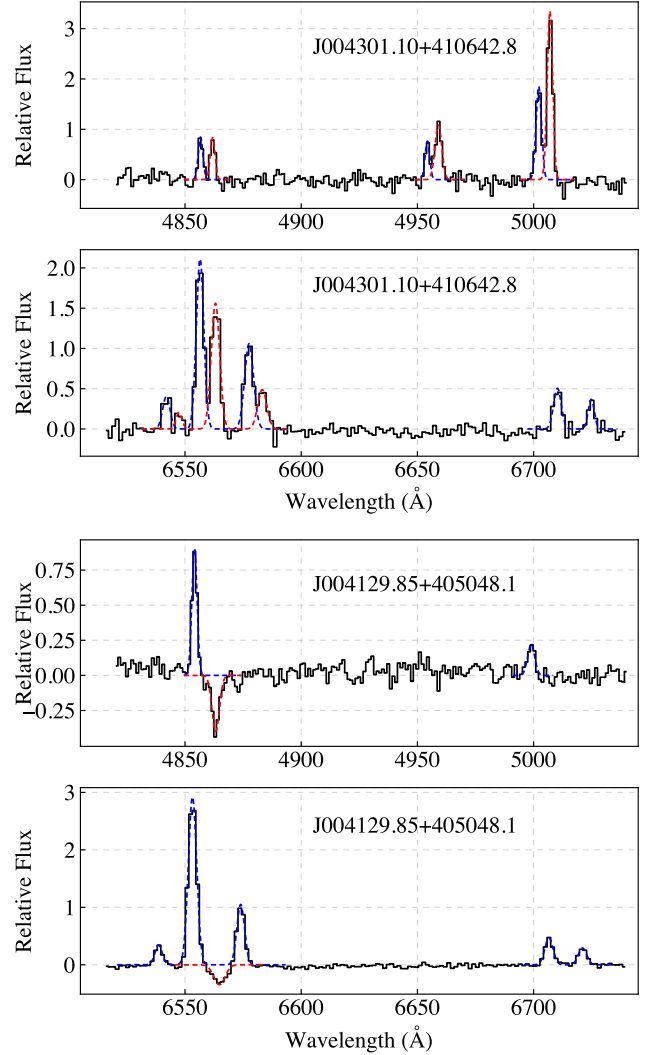


Figure 5. LAMOST spectra of two dual-velocity objects. The two velocity components are color-coded for clarity: blue indicates the blueshifted component, while red signifies the redshifted. Object J004301.10+410642.8 (top two panels), a PN candidate from M06, shows a velocity disparity of $\sim 280 \text{ km s}^{-1}$. Object J004129.85+405048.1 (bottom two panels), identified as an H II region in M31, displays a velocity difference of 528 km s^{-1} .

based on its strong [N II] nebular emission lines. However, the classification of this object might be affected by contamination from the emission of diffuse ionized gas, as the object lies very close to the bulge region of M31. These overlapping objects are marked in Table 3.

5.1.1. Relative Line Fluxes and Radial Velocities

To characterise spectral features and refine the classification of emission-line nebulae, we measured the radial velocities and fluxes of several emission lines for each object in our catalog. These lines include H β , [O III] $\lambda\lambda 4959, 5007$, H α , [N II] $\lambda\lambda 6548, 6584$, and [S II]

Table 3. Emission-line Nebulae in M31 and M33 Identified from the LAMOST Database

Designation	R.A. (J2000)	Decl. (J2000)	M06 ID ^a	M06 V_r ^b (km s ⁻¹)	B24 ID ^c	V_r (km s ⁻¹)
J004553.35+420850.4	11.47233	42.14734	32	-70.3		-72.1 ± 9.6
J004634.35+421143.2	11.64315	42.19534	57	-51.9	287	-74.1 ± 0.2
J004610.59+421244.3	11.54413	42.21231	60	-66.3		-76.0 ± 0.3
...
J004024.70+413727.9	10.10292	41.62444	3222	-224.1		-222.0 ± 1.7
J004257.00+405101.8	10.73750	40.85050	3239	-160.1		-155.2 ± 2.2
J004047.70+413729.4	10.19875	41.62486	3247	-387.1		-380.2 ± 29.3
...
J013255.98+303426.7	23.23326	30.57410				-137.1 ± 1.7
J013301.32+303044.1	23.25553	30.51226				-128.3 ± 0.4
J013415.68+303346.1	23.56536	30.56281				-164.6 ± 1.2
...

blue V_r (km s ⁻¹)	red V_r (km s ⁻¹)	N2	O3	Host	Literature ^d	Classification ^e	Comments
-72.0 ± 10.0	-74.2 ± 34.7	-2.0	2.0	M31	PN	PN	
-63.0 ± 0.3	-95.5 ± 0.4	-0.82	0.43	M31	HII	HII	
-73.6 ± 0.3	-113.9 ± 1.3	-0.7	0.2	M31	HII	HII	
...
-223.1 ± 1.9	-217.0 ± 4.0	-0.83	1.41	M31	PN	PN	NGC 205?
-151.5 ± 3.7	-157.2 ± 2.8	-0.1	0.58	M31	PN _c	PN _c	M32?
-380.2 ± 29.3			2.0	M31	PN _c	PN _c	NGC 205?
...
-128.2 ± 7.5	-137.6 ± 1.8	-0.54	-2.0	M33		HII _c	
-127.1 ± 0.7	-128.7 ± 0.4	-0.63	0.32	M33	HII	HII	
-167.4 ± 4.5	-164.4 ± 1.3	-0.58	-0.18	M33		HII _c	
...

^a Object ID given in Merrett et al. (2006).

^b Radial velocity given in Merrett et al. (2006).

^c Object ID given in Bosomworth et al. (2024).

^d Classification from the literature; candidate objects are marked as “*_c”.

^e New classification made in this work based on the LAMOST database.

NOTE—This table is published in its entirety online only in the machine-readable format.

$\lambda\lambda 6716, 6731$, when available. A linear continuum was fitted within a $\sim 20 \text{ \AA}$ range, and each line was modeled with a Gaussian profile. The central wavelength of the fit determined the line’s radial velocity, while line fluxes were extracted by integrating the area under the Gaussian after subtracting the continuum.

In regions where emission lines are blended (e.g., $6545 \sim 6590 \text{ \AA}$), we applied a method similar to Prichard et al. (2017), fitting simultaneous Gaussian profiles using the equation:

$$f(x) = (mx + c) + \frac{A_1}{\sigma_1 \sqrt{2\pi}} \exp\left(-\frac{(x - \lambda_1)^2}{2\sigma_1^2}\right) + \frac{A_2}{\sigma_2 \sqrt{2\pi}} \exp\left(-\frac{(x - (\lambda_1 + \Delta\lambda))^2}{2\sigma_2^2}\right), \quad (5)$$

where m and c describe the continuum, A_1 and A_2 are the amplitudes of the two peaks, and σ_1 and σ_2 represent their widths. λ_1 is the central wavelength of the first emission line, and $\Delta\lambda$ is the separation between the two lines, based on the systemic velocities of M31 and M33. This method proved more accurate than fitting each line independently, as it reduced the number of free parameters, though slight velocity shifts might be introduced.

Given LAMOST’s large fiber diameter, contamination from external sources, such as foreground stars or diffuse ionized gas in M31, is inevitable. This issue is particularly pronouncing near the spiral arms and bulge regions, where contamination may render line-fitting unre-

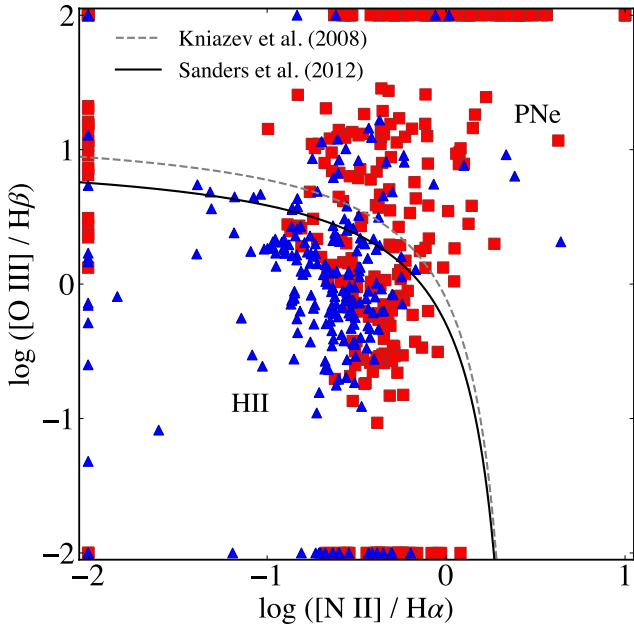


Figure 6. BPT diagram of the emission-line nebulae in our catalog. The nebulae in M31 are shown as red squares, and those in M33 as blue triangles. The black solid line represents our criterion for distinguishing PNe from H II regions. The grey dashed line reflects the demarcation given by Kniazev et al. (2008).

liable. Occasionally, a secondary velocity component is evident in the spectra, as shown in Fig. 5. In such cases, we provided comments in the catalog and reported the velocities and fluxes consistent with previous literature.

The final radial velocity for each object was calculated as the weighted average of the velocities from individual emission lines, with weights inversely proportional to the error in each measurement. In some cases, discrepancies between the blue- and red-arm spectra radial velocities were observed, likely due to LAMOST’s wavelength calibration. To account for this, we separately provided velocities derived from the blue- and red-arm spectra, ensuring careful interpretation of these values. A comparison with M06 velocities for 171 common objects revealed a mean difference of -3.54 km s^{-1} and a standard deviation of 18.28 km s^{-1} .

5.1.2. Final Classification

At a distance of approximately 800 kpc, most emission-line nebulae appear as point sources in LAMOST data, except for a few extended H II regions. This complicates morphological classification, making spectral features essential for identification. These features include forbidden emission lines from elements like oxygen, nitrogen, and sulfur, as well as hydrogen recombination lines. We used the Baldwin-Phillips-Terlevich

(BPT; Baldwin et al. 1981) diagram (Fig. 6), which differentiates PNe from H II regions based on the line ratios of $[\text{O III}] \lambda 5007 / \text{H}\beta$ (O3) and $[\text{N II}] / \text{H}\alpha$ (N2). Here, $[\text{N II}]$ represents the combined flux of the lines at 6548 Å and 6583 Å.

While other diagnostic diagrams exist (Frew & Parker 2010), incorporating red sulfur lines at $\lambda\lambda 6716, 6731 \text{ Å}$, these lines are often weak in LAMOST spectra, which could introduce ambiguity due to low S/N. The BPT diagram is preferred because it uses lines of similar wavelengths, minimizing the effects of extinction, reddening, and flux calibration errors. As shown in Fig. 6, some sources are plotted on the boundaries of the BPT diagram. This distribution is primarily due to the very low emission-line strengths observed in their LAMOST spectra. For example, sources found at the lower edge of the diagram exhibit $[\text{O III}] \lambda 5007$ line intensities close to zero, resulting in O3 values near zero, which places them at the lower boundary. Conversely, sources at the upper edge of the diagram show almost no detectable H β emission, causing their O3 values to approach infinity, and we have plotted them accordingly at the upper boundary of the diagram.

To distinguish the PNe and H II regions from the BPT diagram, we adopted the criterion from Sanders et al. (2012), specifically:

$$\text{O3} > (0.61 / (\text{N2} - 0.47)) + 1.0. \quad (6)$$

In addition to using the BPT diagram, we visually inspected objects near the classification boundary to confirm their final types. As a result, 321 objects were classified as H II regions and 269 as PNe. A small number of objects could not be classified due to low S/N, particularly in the blue-arm spectra, and were labeled as “Unknown” in our catalog.

It’s important to note that H II regions often coincide with young, massive blue stars, which can raise the blue-arm continuum and introduce absorption components into the Balmer emission lines. This effect slightly reduces the measured intensities of these lines. Given LAMOST’s $\sim 3''$ fiber diameter, this issue is exacerbated. However, we believe the classification remains reliable, as the Balmer emission lines in these spectra are generally much stronger than the $[\text{O III}] \lambda\lambda 4959, 5007$ lines, indicating low-excitation environments.

5.1.3. Spatial Distribution

Fig. 7 shows the spatial distribution of all classified emission-line nebulae. In M31, PNe are spread across a wide region, from the bulge to the halo. Several PNe are spatially associated with known substructures revealed by the PAndAS survey (McConnachie et al. 2018), such

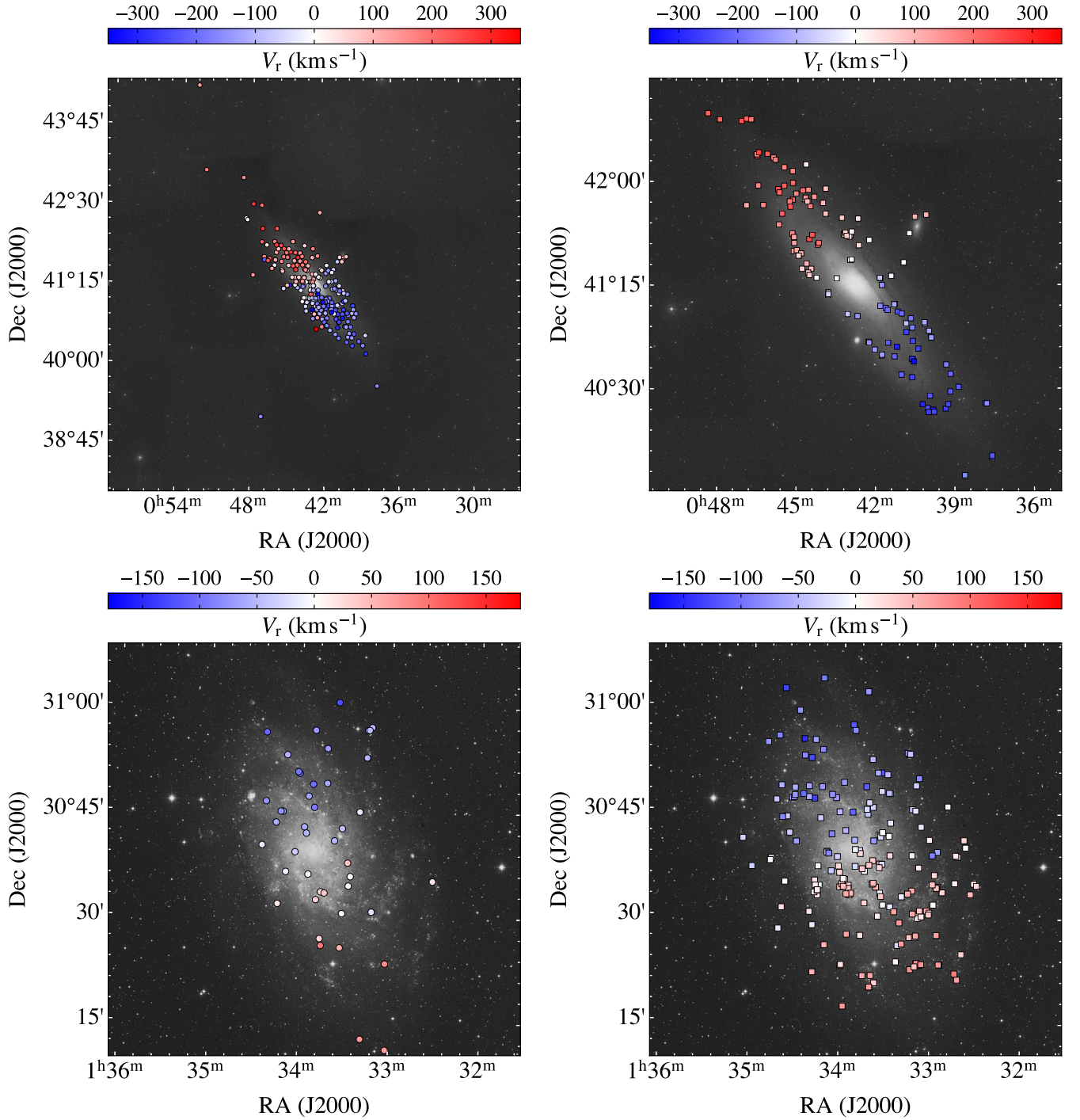


Figure 7. Spatial distributions of classified emission-line nebulae observed with LAMOST, overlaid on the mosaicked images of M31 and M33 as retrieved from the Digitized Sky Survey. Top panels: spatial distributions of PNe (left panel, little circles) and H II regions (right panel, little squares) in M31. Bottom panels: same as top, but for M33. Color-coding of the data symbols represents weighted radial velocity after subtracting the systemic velocity (V_r) of the host galaxy. A systemic velocity of -179 km s^{-1} for M33 was adopted.

as the Giant Stellar Stream and the Northern Clump. H II regions trace the spiral structure of M31, particularly the star-forming ring at a radius of about 10 kpc. The velocity distribution of H II regions closely follows M31’s rotation, while PNe exhibit a more random distribution, reflecting a higher level of asymmetric drift.

We also identified a few objects likely associated with NGC 221 (M32), NGC 205, and Andromeda IV, based on their positions and radial velocities. For these objects, we added comments in the catalog. Among them, three H II region candidates are located in NGC 205’s halo. These may be low-excitation PNe or symbiotic binaries, requiring confirmation via deep spectroscopy.

In M33, the PNe and H II regions detected by LAMOST are confined to the optical disk. The H II regions clearly trace the spiral arms, though further verification through chemical analysis and more accurate velocity measurements is needed. The number of H II regions in M33 exceeds that of PNe, likely due to the larger physical size of H II regions, which increases the likelihood of detection with LAMOST fibers. In contrast to M31, no PNe or candidates were found in M33’s halo, consistent with previous studies (Galera-Rosillo et al. 2018).

5.2. Star Clusters

We compiled a catalog of 344 confirmed star clusters and 36 cluster candidates in M31 after excluding the low-SN spectra as well as those with galaxy-like features. The known star clusters in M33 were excluded from the catalog. These clusters span a wide range of locations in M31, from the bulge to the outer halo. Table 4 lists the names, positions, radial velocities, and classification status of these objects. Most of the sources were drawn from the RBC V5 and the Panchromatic Hubble Andromeda Treasury (PHAT) survey (Dalcanton et al. 2012; Johnson et al. 2012, 2015). However, 51 objects classified as GC candidates in the RBC V5, which exhibited large redshifts characteristic of galaxies, were excluded from our final catalog. Another notable case is LAMOST J004251.86+404409.8 (SK055A in RBC V5), previously classified as a confirmed GC, but now reclassified as a background galaxy based on its redshift of $z \approx 0.18$.

Additionally, some spectra from previously known clusters, both young and old, displayed emission lines of varying strength. Those with weak continua and strong Balmer emission lines were reclassified as H II regions. These regions, often populated by young stars, show slightly extended morphologies and are unlikely to evolve into older, gravitationally bound clusters due to their weaker stellar associations. In the remaining spectra, the weaker emission features are likely due to either

the clusters themselves or the diffuse ionized gas present in M31’s disk or bulge.

Upon reviewing PAndAS images of a subset of cluster candidates identified through our RFC predictions, we found no new candidates with obvious extended morphologies. Nonetheless, a few compact, unresolved clusters may remain undetected. Future space-based telescopes, such as the China Space Station Telescope (CSST; Zhan 2011, 2018), are expected to shed light on these remaining objects.

5.3. Supergiant Candidates

Our final catalog of M31 supergiants, identified from the LAMOST spectroscopy, contains 375 objects. Recently, Wu et al. (2024) carried out a systematic identification of supergiants in M31 and M33 using the LAMOST data, resulting in 199 supergiant candidates in M31 in the “Rank1” and “Rank2” classes. Of these, 86 objects are common in both their catalog and ours. In comparison with their methods, we adopted the updated position-velocity relation from Massey & Evans (2016) and arrived at a more strict criterion in velocity (see Sect. 4.1). In addition, we focused our analysis on a smaller region with galactocentric radius $R_{\text{gal}} < 25$ kpc. However, we chose not to apply photometric and astrometric cuts, since the process could cause loss of some targets.

Based on their findings, we have updated the status of these objects in our catalog, reclassifying 56 common individuals from new candidates to known supergiant candidates. In addition, we incorporated 40 objects from the “Stars in the M31 Catalog” provided by Nelson Caldwell as known candidates. Due to their high luminosity, which makes them detectable by LAMOST, these objects are likely supergiant candidates. In total, our supergiant catalog includes 183 supergiants and candidates documented in previous studies, as well as 192 newly identified supergiant candidates. We cross-matched our objects with the LGGS photometry catalog (Massey et al. 2006) using a radius of $3''$ to obtain additional magnitude and color information. The basic properties of these objects are summarized in Table 5.

Despite that M31 is located along the direction of northern Galactic halo, contamination from the MW foreground stars remains significant. Drout et al. (2009) restricted yellow supergiant candidates to radial velocities < -150 km s $^{-1}$ to estimate contamination of foreground stars. This approach aligns well with our result of a 3σ boundary for the MW objects ($V_r < -149.5$ km s $^{-1}$). While efficient in filtering out Milky Way disk stars, this criterion is less so for the stars in the Galactic halo. Since a significant portion of M31’s

Table 4. Star Clusters in M31 Identified from the LAMOST Database

Name	R.A. (J2000)	Decl. (J2000)	RBC V_r	Caldwell V_r (km s^{-1})	V_r^a	APID ^b	Status ^c
B001	9.96253	40.96963	-179	-203.3	-209.1 ± 6.0		1
B002	10.01072	41.19822	-338	-338.2	-336.3 ± 32.0		1
B003	10.03917	41.18478	-351	-377.0	-329.5 ± 11.1		1
B004	10.07468	41.37786	-369	-369.8	-374.3 ± 1.4		1
B005	10.08462	40.73287	-265	-291.6	-292.5 ± 6.9		1
...
B370	11.31000	41.96132	-352	-352.7	-382.1 ± 4.7	1773	1
B372	11.38908	42.00678	-216	-226.9	-242.9 ± 5.8	545	1
B373	11.42436	41.75929	-219	-216.2	-228.9 ± 1.4	1920	1
...
SK168B	11.10958	40.25143			-67.8 ± 7.4		2
SK214B	11.47515	39.94646			-104.8 ± 9.7		2
SK223B	11.63737	40.11049			-138.2 ± 4.0		2
...

^aRadial velocity from LAMOST.

^bAndromeda project identification number in [Johnson et al. \(2015\)](#).

^cClassification status (1: confirmed star cluster, 2: candidate star cluster)

NOTE—This table is published in its entirety online only in the machine-readable format.

Table 5. Supergiants in M31 Identified from the LAMOST Database

Designation	R.A. (J2000)	Decl. (J2000)	V_r (km s^{-1})	V_{exp} (km s^{-1})	R_{gal} (kpc)	P_{M31}	P_{MW}	V (mag)	$B - V$ (mag)	Type ^a	W24 ^b
J004207.85+405152.1	10.53273	40.86448	-452.8 ± 6.5	-411.9	10.9	0.9012	0.0	16.988	0.761	ysg	1
J004247.29+414451.0	10.69708	41.7475	-262.6 ± 3.3	-225.7	18.2	0.9185	0.0	16.410	0.465	ysg	1
J004120.56+403514.6	10.33567	40.58741	-438.0 ± 4.9	-439.7	15.9	0.9999	0.0	17.099	0.599	ysg	
J004428.08+415503.0	11.11704	41.91751	-136.2 ± 1.5	-117.0	13.1	0.9768	0.0273	16.773	2.046	rsg	1
J004731.11+422748.8	11.87966	42.46357	-91.1 ± 1.5	-55.6	20.4	0.9243	0.2720	17.354	2.061	rsg_c	
...
J003913.02+401655.5	9.80425	40.28211	-504.8 ± 3.8	-527.3	16.8	0.9706	0.0	18.307	-0.009	sg_c	
J004235.77+405855.8	10.64904	40.98217	-353.0 ± 58.3	-375.0	10.0	0.9717	0.0	19.202	0.29	sg_c	
J004503.67+413708.5	11.26533	41.61903	-106.9 ± 6.6	-142.8	10.6	0.9258	0.1389	16.151	0.176	sg_c	
...
J003853.73+403830.2	9.72390	40.64173	-512.8 ± 6.5	-474.2	17.2	0.9113	0.0	18.441	0.143	star	
J004205.31+410254.0	10.52213	41.04835	-498.5 ± 5.7	-493.2	4.1	0.9980	0.0	18.829	0.112	star	1
J004505.51+414658.3	11.27296	41.78288	-67.6 ± 7.5	-57.5	9.4	0.9934	0.5734	17.096	0.276	star	
...

^aClassification type: known supergiants are labeled with types as reported in literature, and candidates are denoted with “_c”. “sg_c” represents new candidates identified in this study. Objects in the “Stars in the M31 Catalog” are labeled as “star”.

^bObjects labeled with “1” indicate common entries identified in [Wu et al. \(2024\)](#).

NOTE—This table is published in its entirety online only in the machine-readable format.

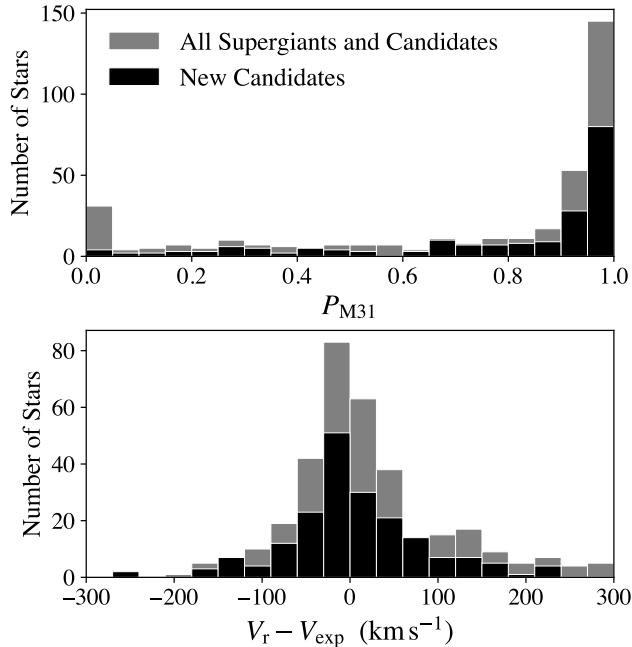


Figure 8. Top: Distribution of the probability of M31 membership (P_{M31} , values scaled from 0 to 1) of our newly identified supergiant candidates (in black), along with known supergiants and candidates (in grey). Bottom: Distribution of ($V_r - V_{exp}$) for the known and newly identified supergiants and candidates, with the same color-coding as above.

systemic radial velocity is influenced by the relative motion of the Sun, some Galactic halo stars can exhibit large negative radial velocities that mimic M31’s motion, complicating our exclusion of these object from the sample. As such, stars from the Galactic halo are the primary source of contamination in our data.

To address this, we employed a likelihood-based approach that differentiates between foreground stars and those belonging to M31 by considering both velocity and positional information. An object is assigned a higher probability of belonging to M31 if its observed radial velocity aligns closely with the expected velocity, which is calculated based on its position in M31’s deprojected disk plane. However, the 3σ boundary is a conservative criterion. The circular velocities of short-lived supergiants are expected to closely follow M31’s rotation velocity, except for a few runaway stars (Evans & Massey 2015). Among the new candidates identified through radial velocity, 152 fall within the 1σ confidence interval, while 32 lie between the 1σ and 2σ interval. As P_{M31} decreases, the likelihood of contamination from Galactic halo stars increases. Fig. 8 shows the probability distribution of our sample, highlighting that a subset of previously identified objects has a low likelihood of

M31 membership. Caution is advised when interpreting these results.

Fig. 9 illustrates the spatial distribution of all known supergiants and candidates, with color indicating their P_{M31} values (ranging from 0 to 1). Seven known supergiants with uncertain velocity measurements, along with objects from the “Unknown” spectra lacking redshift data, are shown in white. The objects span a galactocentric distance (R_{gal}) from 0 to 25 kpc to the center of M31. While most high-probability M31 members are spatially correlated with the spiral arms of M31, we also detect outliers in the outskirts of the disk. Notably, several high-confidence candidates are located in the southwestern quadrant of the disk, extending beyond the main spiral arms. These are likely associated with the arc-like structures seen in infrared and H I images (Fritz et al. 2012; Chemin et al. 2009; Braun et al. 2009). A few H II regions are also located in this area (see Fig. 7). These objects provide valuable insight into the outskirts of M31, and follow-up high-resolution spectroscopy could help further investigate their nature, shedding light on the chemical evolution and nucleosynthetic history of these extended structures.

Interestingly, the distribution of objects in Fig. 9 shows a higher concentration to the right. This pattern is a consequence of M31’s rotation, as objects in the northeastern part of the disk are expected to have radial velocities $V_{exp} > -150$ km s⁻¹ (i.e., $X/R_{gal} \gtrsim 0.67$ in Equation 4). As a result, many of these objects blend with foreground disk stars and were excluded from our final sample to reduce contamination. A promising approach to mitigate this bias involves using spectral features identified through high-resolution spectroscopy, which can more reliably separate M31 supergiants from foreground stars (e.g. Massey et al. 2016; Gordon et al. 2016).

6. SUMMARY

We employed an RFC model to first classify all LAMOST spectra, categorizing objects into three groups, non-emission stars, star cluster candidates, and emission-line objects. For the spectra that could not be classified using the RFC model, we conducted detailed visual inspection, focusing on identifying potential emission-line nebulae and supergiant candidates with broad emission lines. High-quality g - and i -band images from the PAndAS survey were collected and visually checked for star cluster candidates with RF scores exceeding 0.95. Subsequently, emission-line nebulae and emission-line stars were distinguished based on their continuum levels in the spectra. For all emission-line nebulae, we systematically measured radial velocities

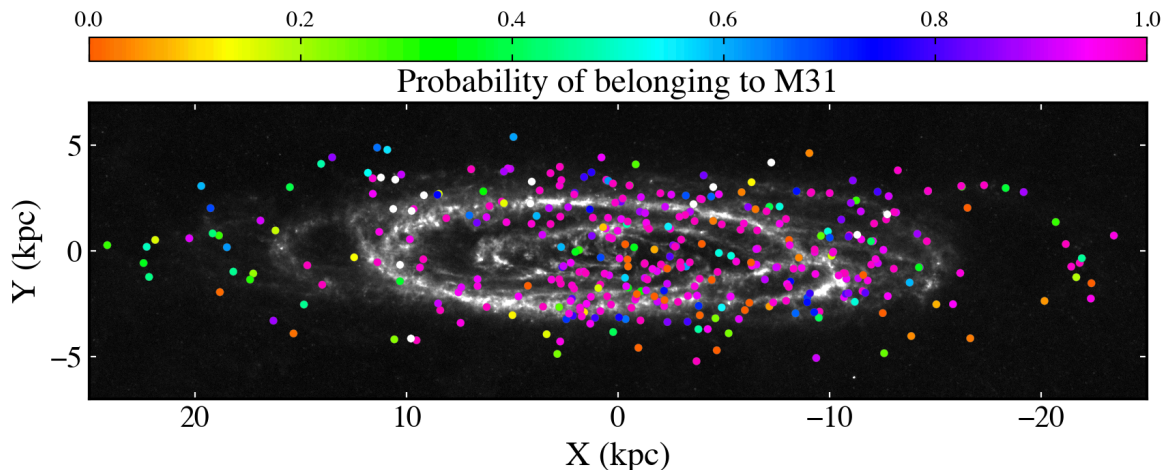


Figure 9. Spatial distribution of supergiants and candidates in M31 as identified from the LAMOST database, overlaid on the *Herschel* SPIRE 250 μm image (Fritz et al. 2012). Objects are color-coded according to the probability of M31 membership (P_{M31} , values scaled from 0 to 1); a few objects that lack accurate radial velocity information are shown in white.

from prominent nebular emission lines and further classified them as planetary nebulae (PNe) or H II regions, using emission-line ratio diagnostics. Using spatial position and the radial velocity as measured from the LAMOST spectra, we compared the observed velocities of the remaining objects with those predicted by M31’s rotational pattern. Two Gaussian functions were constructed to estimate the likelihood of an object being associated with M31 or the MW based on kinematic data. We then selected new supergiant candidates by applying a set of criteria.

As a result, we present a comprehensive catalog of 1139 unique objects in M31, observed by LAMOST. These objects are classified into three main categories: emission-line nebulae, star clusters, and supergiants, encompassing both confirmed and candidate members. As part of our survey, we also identified 245 emission-line nebulae in M33. Since M31 is no longer part of LAMOST’s current observational plan (Phase 3), this catalog represents a definitive record of all confirmed and candidate members identified from the released LAMOST data on M31. Many of the objects in M31 and M33 were initially identified through photometric surveys (e.g., H II regions). The addition of LAMOST spectra provides essential complementary data, allowing us to better characterize their nature. The cataloged objects serve as valuable tracers for studying the chemical composition, kinematics, and stellar populations of our

neighboring galaxies, offering key insights into their formation and evolutionary history.

ACKNOWLEDGEMENTS

We are grateful to the anonymous referee whose excellent comments and suggestions greatly improved this article. This work is partially supported by the National Natural Science Foundation of China 12173034 and 12322304, the National Natural Science Foundation of Yunnan Province 202301AV070002 and the Xingdian talent support program of Yunnan Province. We acknowledge the science research grants from the China Manned Space Project with NO. CMS-CSST-2021-A09, CMS-CSST-2021-A08 and CMS-CSST-2021-B03.

The emission-line fitting procedure was performed using *Scipy* (Virtanen et al. 2020) and *Specutils* (Earl et al. 2022).

Guoshoujing Telescope (LAMOST – Large Sky Area Multi-Object Fiber Spectroscopic Telescope) is a National Major Scientific Project built by the Chinese Academy of Sciences. Funding for the project has been provided by the National Development and Reform Commission. LAMOST is operated and managed by the National Astronomical Observatories, Chinese Academy of Sciences.

DATA AVAILABILITY

The complete catalogs are published in their entirety online in the machine-readable format, and also available in electronic forms at the CDS.

REFERENCES

Alexeeva, S., & Zhao, G. 2022, *ApJ*, 925, 76, doi: [10.3847/1538-4357/ac38ab](https://doi.org/10.3847/1538-4357/ac38ab)

Baldwin, J. A., Phillips, M. M., & Terlevich, R. 1981, *PASP*, 93, 5, doi: [10.1086/130766](https://doi.org/10.1086/130766)

- Battistini, P., Bonoli, F., Braccési, A., et al. 1987, *A&AS*, 67, 447
- Bernat, A. P., & Lambert, D. L. 1978, *PASP*, 90, 520, doi: [10.1086/130376](https://doi.org/10.1086/130376)
- Bhattacharya, S., Arnaboldi, M., Gerhard, O., et al. 2021, *A&A*, 647, A130, doi: [10.1051/0004-6361/202038366](https://doi.org/10.1051/0004-6361/202038366)
- Bhattacharya, S., Arnaboldi, M., Hartke, J., et al. 2019, *A&A*, 624, A132, doi: [10.1051/0004-6361/201834579](https://doi.org/10.1051/0004-6361/201834579)
- Bhattacharya, S., Arnaboldi, M., Caldwell, N., et al. 2022, *MNRAS*, 517, 2343, doi: [10.1093/mnras/stac2703](https://doi.org/10.1093/mnras/stac2703)
- Bosomworth, C., Forbrich, J., Lada, C. J., et al. 2024, *MNRAS*, doi: [10.1093/mnras/stae2805](https://doi.org/10.1093/mnras/stae2805)
- Braun, R., Thilker, D. A., Walterbos, R. A. M., & Corbelli, E. 2009, *ApJ*, 695, 937, doi: [10.1088/0004-637X/695/2/937](https://doi.org/10.1088/0004-637X/695/2/937)
- Breiman, L. 2001, *Machine Learning*, 45, 5, doi: [10.1023/A:1010933404324](https://doi.org/10.1023/A:1010933404324)
- Chemin, L., Carignan, C., & Foster, T. 2009, *ApJ*, 705, 1395, doi: [10.1088/0004-637X/705/2/1395](https://doi.org/10.1088/0004-637X/705/2/1395)
- Chen, B., Liu, X., Xiang, M., et al. 2016, *AJ*, 152, 45, doi: [10.3847/0004-6256/152/2/45](https://doi.org/10.3847/0004-6256/152/2/45)
- Chen, B.-Q., Liu, X.-W., Xiang, M.-S., et al. 2015, *Research in Astronomy and Astrophysics*, 15, 1392, doi: [10.1088/1674-4527/15/8/020](https://doi.org/10.1088/1674-4527/15/8/020)
- Cui, X.-Q., Zhao, Y.-H., Chu, Y.-Q., et al. 2012, *Research in Astronomy and Astrophysics*, 12, 1197, doi: [10.1088/1674-4527/12/9/003](https://doi.org/10.1088/1674-4527/12/9/003)
- Cutri, R. M., Skrutskie, M. F., van Dyk, S., et al. 2003, *2MASS All Sky Catalog of point sources*.
- Dalcanton, J. J., Williams, B. F., Lang, D., et al. 2012, *ApJS*, 200, 18, doi: [10.1088/0067-0049/200/2/18](https://doi.org/10.1088/0067-0049/200/2/18)
- de Vaucouleurs, G. 1959, *ApJ*, 130, 728, doi: [10.1086/146764](https://doi.org/10.1086/146764)
- de Vaucouleurs, G., de Vaucouleurs, A., Corwin, Herold G., J., et al. 1991, *Third Reference Catalogue of Bright Galaxies*
- Dennison, B., Simonetti, J. H., & Topasna, G. A. 1998, *PASA*, 15, 147, doi: [10.1071/AS98147](https://doi.org/10.1071/AS98147)
- Drout, M. R., Massey, P., & Meynet, G. 2012, *ApJ*, 750, 97, doi: [10.1088/0004-637X/750/2/97](https://doi.org/10.1088/0004-637X/750/2/97)
- Drout, M. R., Massey, P., Meynet, G., Tokarz, S., & Caldwell, N. 2009, *ApJ*, 703, 441, doi: [10.1088/0004-637X/703/1/441](https://doi.org/10.1088/0004-637X/703/1/441)
- Earl, N., Tollerud, E., O'Steen, R., et al. 2022, *astropy/specutils: v1.9.1, v1.9.1*, Zenodo, Zenodo, doi: [10.5281/zenodo.7348235](https://doi.org/10.5281/zenodo.7348235)
- Evans, K. A., & Massey, P. 2015, *AJ*, 150, 149, doi: [10.1088/0004-6256/150/5/149](https://doi.org/10.1088/0004-6256/150/5/149)
- Frew, D. J., & Parker, Q. A. 2010, *PASA*, 27, 129, doi: [10.1071/AS09040](https://doi.org/10.1071/AS09040)
- Fritz, J., Gentile, G., Smith, M. W. L., et al. 2012, *A&A*, 546, A34, doi: [10.1051/0004-6361/201118619](https://doi.org/10.1051/0004-6361/201118619)
- Galera-Rosillo, R., Corradi, R. L. M., & Mampaso, A. 2018, *A&A*, 612, A35, doi: [10.1051/0004-6361/201731383](https://doi.org/10.1051/0004-6361/201731383)
- Galleti, S., Federici, L., Bellazzini, M., Fusi Pecci, F., & Macrina, S. 2004, *A&A*, 416, 917, doi: [10.1051/0004-6361:20035632](https://doi.org/10.1051/0004-6361:20035632)
- Gordon, M. S., Humphreys, R. M., & Jones, T. J. 2016, *ApJ*, 825, 50, doi: [10.3847/0004-637X/825/1/50](https://doi.org/10.3847/0004-637X/825/1/50)
- Hillier, D. J. 1991, *A&A*, 247, 455
- Holland, S. 1998, *AJ*, 115, 1916, doi: [10.1086/300348](https://doi.org/10.1086/300348)
- Huang, Y., Zhang, H. W., Wang, C., et al. 2019, *ApJL*, 884, L7, doi: [10.3847/2041-8213/ab430b](https://doi.org/10.3847/2041-8213/ab430b)
- Hubble, E. 1932, *ApJ*, 76, 44, doi: [10.1086/143397](https://doi.org/10.1086/143397)
- Huxor, A. P., Mackey, A. D., Ferguson, A. M. N., et al. 2014, *MNRAS*, 442, 2165, doi: [10.1093/mnras/stu771](https://doi.org/10.1093/mnras/stu771)
- Johnson, L. C., Seth, A. C., Dalcanton, J. J., et al. 2012, *ApJ*, 752, 95, doi: [10.1088/0004-637X/752/2/95](https://doi.org/10.1088/0004-637X/752/2/95)
- . 2015, *ApJ*, 802, 127, doi: [10.1088/0004-637X/802/2/127](https://doi.org/10.1088/0004-637X/802/2/127)
- Kaffe, P. R., Sharma, S., Lewis, G. F., Robotham, A. S. G., & Driver, S. P. 2018, *MNRAS*, 475, 4043, doi: [10.1093/mnras/sty082](https://doi.org/10.1093/mnras/sty082)
- Kent, S. M. 1989, *PASP*, 101, 489, doi: [10.1086/132457](https://doi.org/10.1086/132457)
- Kniazev, A. Y., Pustilnik, S. A., & Zucker, D. B. 2008, *MNRAS*, 384, 1045, doi: [10.1111/j.1365-2966.2007.12540.x](https://doi.org/10.1111/j.1365-2966.2007.12540.x)
- Liu, C., Kudritzki, R.-P., Zhao, G., et al. 2022, *ApJ*, 932, 29, doi: [10.3847/1538-4357/ac69cc](https://doi.org/10.3847/1538-4357/ac69cc)
- Luo, A. L., Zhao, Y.-H., Zhao, G., et al. 2015, *Research in Astronomy and Astrophysics*, 15, 1095, doi: [10.1088/1674-4527/15/8/002](https://doi.org/10.1088/1674-4527/15/8/002)
- Massey, P., & Evans, K. A. 2016, *ApJ*, 826, 224, doi: [10.3847/0004-637X/826/2/224](https://doi.org/10.3847/0004-637X/826/2/224)
- Massey, P., Neugent, K. F., Levesque, E. M., Drout, M. R., & Courteau, S. 2021, *AJ*, 161, 79, doi: [10.3847/1538-3881/abd01f](https://doi.org/10.3847/1538-3881/abd01f)
- Massey, P., Neugent, K. F., & Smart, B. M. 2016, *AJ*, 152, 62, doi: [10.3847/0004-6256/152/3/62](https://doi.org/10.3847/0004-6256/152/3/62)
- Massey, P., Olsen, K. A. G., Hodge, P. W., et al. 2006, *AJ*, 131, 2478, doi: [10.1086/503256](https://doi.org/10.1086/503256)
- Massey, P., Silva, D. R., Levesque, E. M., et al. 2009, *ApJ*, 703, 420, doi: [10.1088/0004-637X/703/1/420](https://doi.org/10.1088/0004-637X/703/1/420)
- McConnachie, A. W., Irwin, M. J., Ferguson, A. M. N., et al. 2005, *MNRAS*, 356, 979, doi: [10.1111/j.1365-2966.2004.08514.x](https://doi.org/10.1111/j.1365-2966.2004.08514.x)
- McConnachie, A. W., Irwin, M. J., Ibata, R. A., et al. 2009, *Nature*, 461, 66, doi: [10.1038/nature08327](https://doi.org/10.1038/nature08327)
- McConnachie, A. W., Ibata, R., Martin, N., et al. 2018, *ApJ*, 868, 55, doi: [10.3847/1538-4357/aae8e7](https://doi.org/10.3847/1538-4357/aae8e7)

- Merrett, H. R., Merrifield, M. R., Douglas, N. G., et al. 2006, *MNRAS*, 369, 120, doi: [10.1111/j.1365-2966.2006.10268.x](https://doi.org/10.1111/j.1365-2966.2006.10268.x)
- Pedregosa, F., Varoquaux, G., Gramfort, A., et al. 2011, *Journal of Machine Learning Research*, 12, 2825
- Prichard, L. J., Guhathakurta, P., Hamren, K. M., et al. 2017, *MNRAS*, 465, 4180, doi: [10.1093/mnras/stw2984](https://doi.org/10.1093/mnras/stw2984)
- Ren, Y., Jiang, B., Yang, M., et al. 2021, *ApJ*, 907, 18, doi: [10.3847/1538-4357/abcda5](https://doi.org/10.3847/1538-4357/abcda5)
- Rubin, V. C., & Ford, W. Kent, J. 1970, *ApJ*, 159, 379, doi: [10.1086/150317](https://doi.org/10.1086/150317)
- Sanders, N. E., Caldwell, N., McDowell, J., & Harding, P. 2012, *ApJ*, 758, 133, doi: [10.1088/0004-637X/758/2/133](https://doi.org/10.1088/0004-637X/758/2/133)
- Veljanoski, J., Mackey, A. D., Ferguson, A. M. N., et al. 2014, *MNRAS*, 442, 2929, doi: [10.1093/mnras/stu1055](https://doi.org/10.1093/mnras/stu1055)
- Virtanen, P., Gommers, R., Oliphant, T. E., et al. 2020, *Nature Methods*, 17, 261, doi: [10.1038/s41592-019-0686-2](https://doi.org/10.1038/s41592-019-0686-2)
- Walterbos, R. A. M., & Kennicutt, R. C., J. 1987, *A&AS*, 69, 311
- Wang, S., Chen, B., & Ma, J. 2021, *A&A*, 645, A115, doi: [10.1051/0004-6361/202039531](https://doi.org/10.1051/0004-6361/202039531)
- Wang, S., Chen, B., Ma, J., et al. 2022, *A&A*, 658, A51, doi: [10.1051/0004-6361/202142169](https://doi.org/10.1051/0004-6361/202142169)
- Wang, Y., Yuan, H., Chen, B., et al. 2023, *ApJ*, 954, 206, doi: [10.3847/1538-4357/ace963](https://doi.org/10.3847/1538-4357/ace963)
- Wu, H., Huang, Y., Zhang, H., et al. 2024, arXiv e-prints, arXiv:2410.19447, doi: [10.48550/arXiv.2410.19447](https://doi.org/10.48550/arXiv.2410.19447)
- Xiang, M., Liu, X., Zhang, M., Yuan, H., & Huo, Z. 2017, in *IAU Symposium*, Vol. 323, Planetary Nebulae: Multi-Wavelength Probes of Stellar and Galactic Evolution, ed. X. Liu, L. Stanghellini, & A. Karakas, 388–389, doi: [10.1017/S1743921317002356](https://doi.org/10.1017/S1743921317002356)
- Yuan, H.-B., Liu, X.-W., Huo, Z.-Y., et al. 2010, *Research in Astronomy and Astrophysics*, 10, 599, doi: [10.1088/1674-4527/10/7/001](https://doi.org/10.1088/1674-4527/10/7/001)
- Zhan, H. 2011, *Scientia Sinica Physica, Mechanica & Astronomica*, 41, 1441, doi: [10.1360/132011-961](https://doi.org/10.1360/132011-961)
- Zhan, H. 2018, in *42nd COSPAR Scientific Assembly*, Vol. 42, E1.16–4–18
- Zhang, M., Chen, B.-Q., Huo, Z.-Y., et al. 2020, *Research in Astronomy and Astrophysics*, 20, 097, doi: [10.1088/1674-4527/20/6/97](https://doi.org/10.1088/1674-4527/20/6/97)